This is a repository copy of *Interfacial synergy of Ni single atom/clusters and MXene enabling semiconductor quantum dots based superior photoredox catalysis*.

White Rose Research Online URL for this paper:
https://eprints.whiterose.ac.uk/222307/

Version: Accepted Version

Interfacial Synergy of Ni Single Atom/Cluster and MXene Enabling Semiconductor Quantum Dots based Superior Photoredox Catalysis

Ming-Yu Qi,[1#] Wei-Yun Xiao,[2#] Marco Conte,[3] Zi-Rong Tang,[2] and Yi-Jun Xu[2,*]

[1] Institute of Fundamental and Frontier Sciences, University of Electronic Science and Technology of China, Chengdu 611731, P. R. China

[2] College of Chemistry, State Key Laboratory of Photocatalysis on Energy and Environment, Fuzhou University, Fuzhou 350116, P. R. China

[3] School of Mathematical and Physical Sciences, University of Sheffield, Sheffield, S3 7HF, UK

[#] These authors contributed equally

Abstract

Semiconductor-based photocatalysis has evolved over the last decade into a prevalent approach for alcohols oxidation to afford the corresponding carbonyl compounds or C–C/C–O coupled products. Nonetheless, photocatalytic oxidative lactonization of diols to lactones still significantly lags behind even though lactones represent a class of ring moieties with excellent biological activities. In this work, we present the high-performance visible-light-mediated lactonization of diols to lactones and H_2 over the $Ti_3C_2T_x$ MXene-supported CdS quantum dots (QDs) with Ni decoration (Ni/CdS/$Ti_3C_2T_x$). $Ti_3C_2T_x$ acts as a two-dimensional platform for immobilizing CdS to promote the separation and migration of charge carriers, while concomitantly the Cd^{2+} confinement effect of $Ti_3C_2T_x$ significantly retards the hole-induced photocorrosion of CdS. The unique modifications of atomically dispersed Ni species are either incorporated as Ni clusters in CdS to accelerate H_2 evolution, or anchored as Ni single atom on $Ti_3C_2T_x$ for the efficient adsorption and cyclization of diols. The optimized Ni/CdS/$Ti_3C_2T_x$ exhibits remarkably enhanced activity for lactones synthesis, which is 80.4 times higher than that of blank CdS, along with excellent selectivity and high durability. This work brings a conceptual idea to overcome the well-known intrinsic drawback of photoinduced decomposition in semiconductor-based photocatalysts, and offers a generic and robust strategy of utilizing atomically dispersed cocatalyst as active sites for efficient and robust photoredox lactones synthesis and H_2 evolution.

KEYWORDS: quantum dots, MXene, alcohols oxidation, lactones synthesis, H_2 production

TOC GRAPHICS
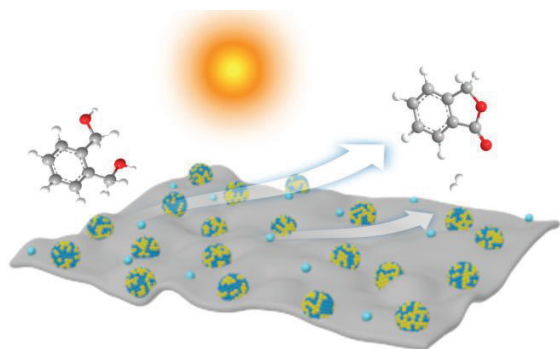
Introduction

Selective oxidation of alcohols represents a fundamental organic transformation of great laboratorial and industrial significance.[1-5] However, conventional noncatalytic methods for the oxidation of alcohols feature a severe drawback, in which toxic and corrosive heavy-metal oxidants, such as permanganate and dichromate, are commonly demanded under harsh operating conditions.[2, 6] Recent years have witnessed a surge in the application of various semiconductor-based catalysts for the photoinduced activation of α/β-C−H, C−O or O−H bonds in alcohols to generate the corresponding carbonyl compounds (i.e., aldehydes and ketones)[3-9] or C–C/C–O coupled products (e.g., ethylene glycol, diethoxyethane and hydrobenzoin)[10-15] under mild reaction conditions. Unfortunately, photocatalytic oxidative lactonization of diols to lactones (i.e., cyclic esters) is still significantly lagging behind even though lactones are versatile motifs found in diverse synthetic and biological architectures,[16-21] with extensive applications in pharmaceutical, food and perfume industries. In general, the conversion of diols to lactones is a tandem reaction involving the sequential cleavage of α-C−H/O−H bonds in diols and the cyclization of subsequently-generated intermediate. The challenges normally associated with this transformation are the difficulties in the unfavorable transannular interaction and cyclization energetics.[22-24] In this scenario, the function-oriented design of semiconductor-based photocatalysts is highly desired to overcome the cyclization barrier, thus breaking the current bottleneck limitation of photo-driven alcohols-to-lactones conversion.

Recently, semiconductor quantum dots (QDs) have showcased supreme privileges in artificial photosystems because of their excellent light harvesting, multiple exciton generation and longer-lived excited states.[11, 25] However, the fast electron-hole recombination, insufficient surface active sites, fussy difficulty in long-term recycling use, and especially intrinsic photoinduced decomposition limit the performance of QDs and in turn, as of now, its technological applicability.[26-28] MXenes as a new two-dimensional (2D) material family of transition metal carbides, nitrides and carbonitrides [29-31], have attracted much attention, among which $Ti_3C_2T_x$ is a prototype with high electrical conductivity, and thus usually serves as an efficient cocatalyst to facilitate the separation and migration of photoinduced charge carriers for significantly enhanced activity over semiconductor-MXenes composite photocatalysts.[31] In particular, taking $Ti_3C_2T_x$ as a 2D platform to construct 0D-2D QDs/$Ti_3C_2T_x$ dot-onto-sheet heterostructures is not only expected to stabilize ultrasmall QDs for high photostability, but also

ensures abundant strong Lewis acid sites for the efficient adsorption and activation of diols.[32-34] Furthermore, considering that transition metal catalysis represents the mainstream in organic chemical cyclization reaction,[23, 35] we reason that the ingenious integration of $Ti_3C_2T_x$-supported semiconductor QDs with transition metal species as surface reaction sites would be a feasible strategy to overcome the cyclization energetics of diols, thereby accomplishing green, durable and high-performance lactones synthesis.

Herein, we report the function-oriented design of $Ti_3C_2T_x$ MXene-supported CdS QDs with Ni decoration (Ni/CdS/$Ti_3C_2T_x$) as the robust and reusable photocatalyst for the highly efficient lactonization of 1,2-benzenedimethanol (1,2-BM) to phthalide integrated with concomitant H_2 production, as displayed in **Figure 1**. In this system, the employed $Ti_3C_2T_x$ nanosheets (NSs) play several significant roles: (i) promoting the separation and migration of charge carriers; (ii) immobilizing CdS QDs to facilitate the recovery of CdS QDs for reuse; (iii) retarding the hole-induced photocorrosion of CdS QDs by the Cd^{2+} confinement effect of $Ti_3C_2T_x$; (iv) offering strong Lewis acid sites for the efficient adsorption and activation of 1,2-BM. More importantly, Ni species are ingeniously incorporated as Ni clusters in CdS QDs to accelerate H_2 evolution, or anchored as Ni single atom on $Ti_3C_2T_x$ NSs for the efficient lactonization of 1,2-BM. Benefiting from these compositional and structural features, as compared to blank CdS QDs, the optimized Ni/CdS/$Ti_3C_2T_x$ composite shows an 80.4-fold enhancement in activity for the phthalide production. Mechanistic studies unveil that the oxygen-centered radicals act as dominant intermediates for lactones synthesis enabled by $Ti_3C_2T_x$-supported single Ni atom assisted radical cyclization process, while the protons abstracted from diols interact with photogenerated electrons for H_2 evolution catalysed by the Ni clusters embedded into CdS QDs. This work highlights an efficient synthetic route of lactones, and is expected to open an avenue of decorating atomically dispersed cocatalysts as the dual active sites onto the semiconductor QDs/MXene heterostructures for achieving semiconductor QDs based robust and recyclable redox catalysis.
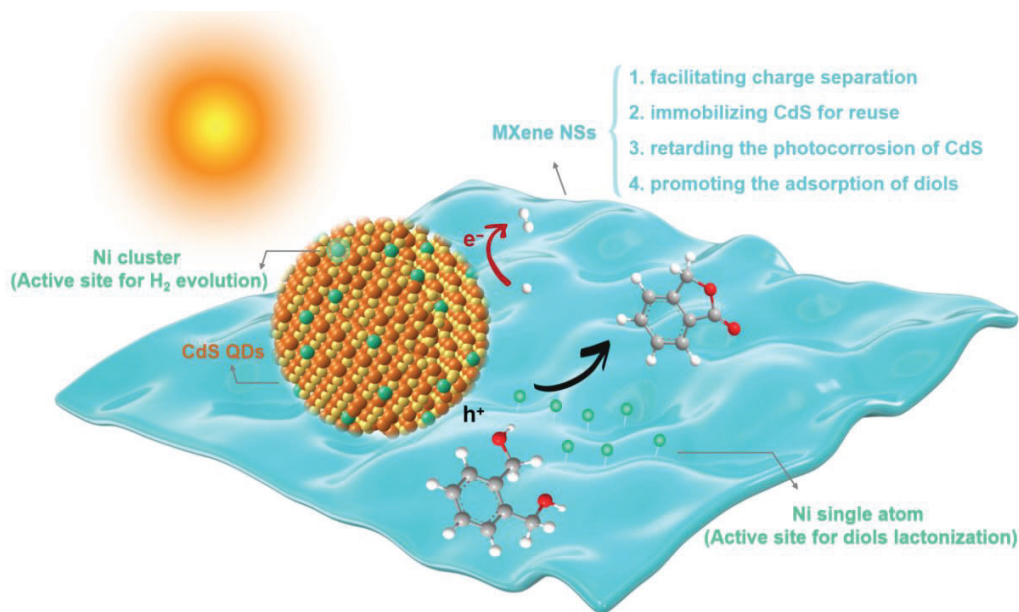
Figure 1. Illustration of using robust and reusable $Ni/CdS/Ti_3C_2T_x$ for highly efficient redox catalysis of diols lactonization integrated with H_2 production under visible light.

Results and Discussion

Preparation and characterization of $Ni/CdS/Ti_3C_2T_x$

Figure 2a shows a schematic diagram of the preparation process of $Ni/CdS/Ti_3C_2T_x$ composites. Firstly, $Ti_3C_2T_x$ nanosheets (NSs) have been successfully prepared according to previous reports (**Figure 2b**).[36] As depicted in **Figure 2c**, the thickness of the $Ti_3C_2T_x$ NSs is approximately 4.83 nm. Subsequently, $Ni/CdS/Ti_3C_2T_x$ has been fabricated by a simple one-pot synthesis method (**Figure 2a**). The transmission electron microscopy (TEM) image (**Figure 2d**) of $Ni/CdS/Ti_3C_2T_x$ shows that the CdS quantum dots (QDs) are homogeneously distributed on the surface of $Ti_3C_2T_x$ NSs, and the ordered lattice stripes with a *d*-spacing of 0.335 nm can be observed in the high-resolution TEM (HR-TEM) image (**Figure 2e**), which correspond to the (111) crystal plane of cubic CdS.[28] From the aberration-corrected high-angle annular dark-field scanning TEM (HAADF-STEM), bright dots corresponding to atomically dispersed Ni atoms are observed in both $Ti_3C_2T_x$ and CdS regions, and no Ni-derived nanoparticles can be found (**Figure 2f**). The dispersion and configuration of Ni species in $Ni/CdS/Ti_3C_2T_x$ were further determined by atomic-resolution element mapping results. As sketched in **Figure 2g**, the uniform distribution of CdS QDs throughout the $Ti_3C_2T_x$ support masks the Ti and C signals, while the

5

dotted distribution of Ni element confirms the atomically dispersed Ni species on the surface of CdS/Ti$_3$C$_2$T$_x$.
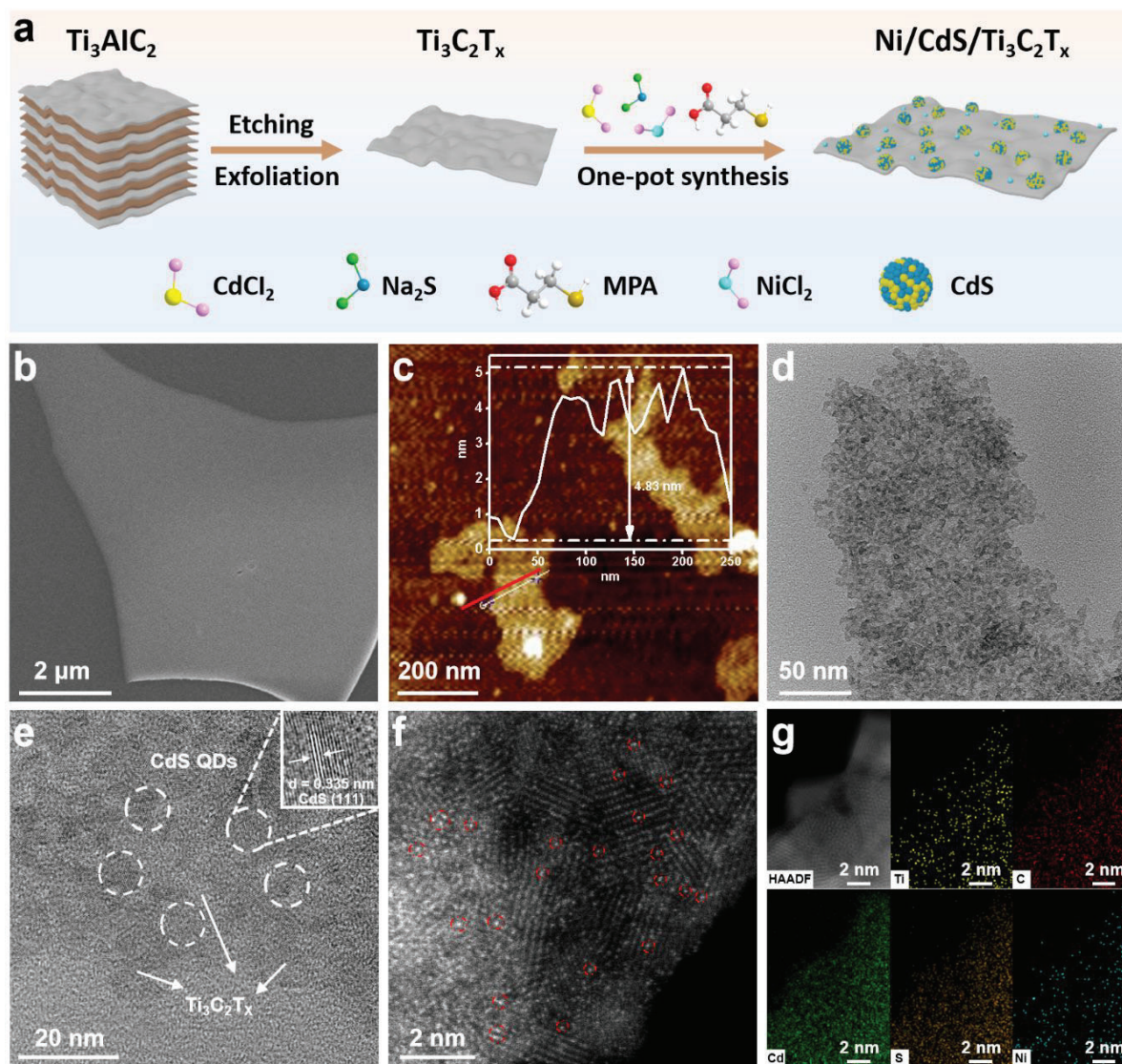
Figure 2. (a) Schematic illustration of the fabrication of Ni/CdS/Ti$_3$C$_2$T$_x$. (b) Scanning electron microscopy image and (c) Atomic force microscopy (AFM) image of Ti$_3$C$_2$T$_x$. (d) TEM image, (e) HR-TEM image and (f) Aberration-corrected HAADF-STEM image of Ni/CdS/Ti$_3$C$_2$T$_x$. (g) HAADF-STEM image and the atomic-resolution element mapping results of Ni/CdS/Ti$_3$C$_2$T$_x$.

The X-ray diffraction (XRD) pattern was performed to identify the crystal structures of the prepared samples. As disclosed in **Figure 3a**, the three diffraction peaks of blank CdS QDs at 26.55°, 44.05° and 51.61° are attributed to the (111), (220) and (311) planes of cubic phase CdS

(JCPDS no. 75-0581), respectively.[11] The XRD spectra of CdS/Ti$_3$C$_2$T$_x$ and Ni/CdS/Ti$_3$C$_2$T$_x$ composites are similar to those of the blank CdS QDs, and no other significant characteristic peaks are observed due to the low contents and homogeneous dispersion of Ni and Ti$_3$C$_2$T$_x$ in the composites. As displayed in the X-ray photoelectron spectroscopy (XPS) survey spectrum (**Figure 3b**), the relevant elements in Ni/CdS/Ti$_3$C$_2$T$_x$ composites can be detected. As shown in **Figure S1b**, the doublet peaks at 411.3 and 404.5 eV are ascribed to the binding energies of Cd 3d$_{3/2}$ and 3d$_{5/2}$ orbits for the +2 oxidation state.[11] **Figure S1c** shows a pair of peaks at 162.3 and 161.0 eV, which are associated with the contribution of S^{2-}.[11] Furthermore, the binding energy of Ni 2p$_{3/2}$ in Ni/CdS/Ti$_3$C$_2$T$_x$ appears at 855.2 eV (**Figure S1d**), which is slightly lower than that of Ni^{2+} state, suggesting that the Ni species in Ni/CdS/Ti$_3$C$_2$T$_x$ are likely to be in a low-valent state.[37]
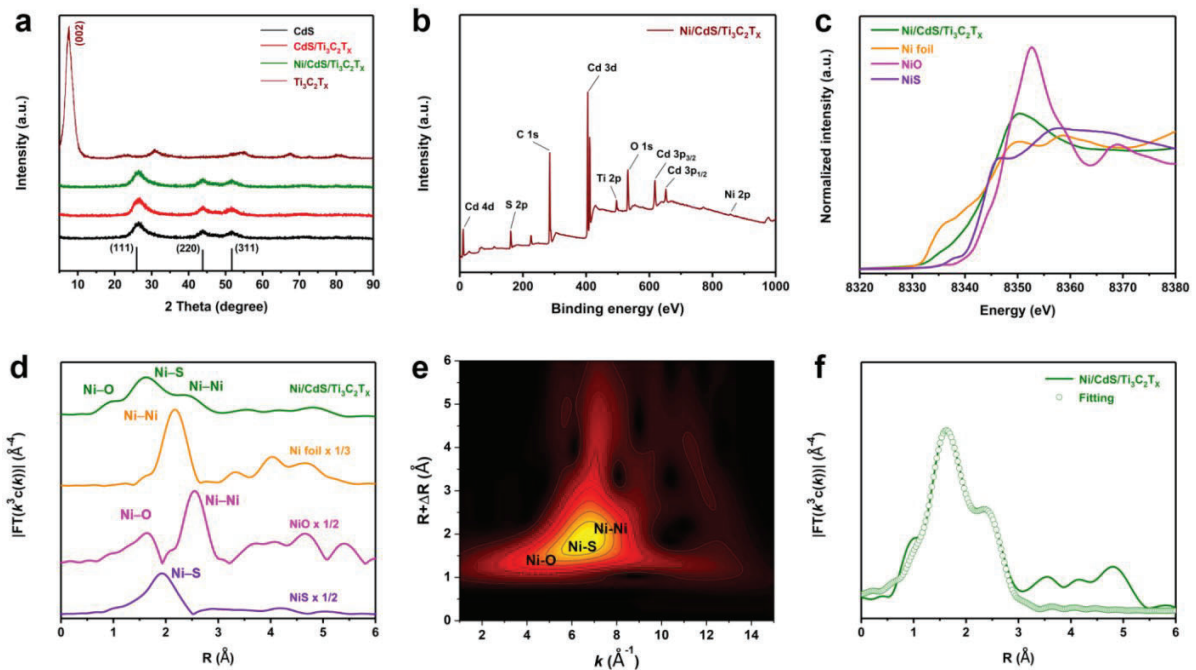
Figure 3. (a) XRD patterns of CdS, CdS/Ti$_3$C$_2$T$_x$, Ni/CdS/Ti$_3$C$_2$T$_x$ and Ti$_3$C$_2$T$_x$. (b) XPS survey spectrum of Ni/CdS/Ti$_3$C$_2$T$_x$. (c) Normalized Ni K-edge XANES spectra of Ni/CdS/Ti$_3$C$_2$T$_x$ in reference to Ni foil, NiO and NiS. (d) FT-EXAFS spectra of Ni/CdS/Ti$_3$C$_2$T$_x$ in reference to Ni foil, NiO and NiS. (e) Wavelet transform for Ni K-edge EXAFS spectra of Ni/CdS/Ti$_3$C$_2$T$_x$. (f) EXAFS fitting curves for Ni/CdS/Ti$_3$C$_2$T$_x$.

The local coordination environment of Ni species was further investigated by X-ray absorption spectroscopy (XAS) measurements. **Figure 3c** shows the Ni K-edge X-ray absorption near-edge structure (XANES) spectrum of Ni/CdS/Ti$_3$C$_2$T$_x$, along with Ni foil, NiO and NiS as references. It is evident that the threshold energy (E$_0$) and XANES white line peak of the Ni K-edge for Ni/CdS/Ti$_3$C$_2$T$_x$ are between those of standard Ni foil and NiO, manifesting that the Ni species in Ni/CdS/Ti$_3$C$_2$T$_x$ is present in an electron-deficient state of Ni$^{\delta+}$ ($0 < \delta < 2$).[38] At the Fourier transform (FT)-extended X-ray absorption fine structure (EXAFS) spectrum of Ni/CdS/Ti$_3$C$_2$T$_x$ (**Figure 3d**), the first coordination peak appearing at about 2.03 Å is attributed to Ni–O contribution, resulting from the single Ni atoms conjugating with the −OH terminal groups on the surface of Ti$_3$C$_2$T$_x$ support.[36] Another two higher coordination peaks at ~2.43 and 2.65 Å are detected, indicating the presence of Ni–S and Ni–Ni contributions derived from ultrasmall Ni clusters embedded into host CdS QDs, which is further confirmed by the Wavelet transform contour plot (**Figure 3e** and **Figure S2**). Quantitative coordination structural results extracted from EXAFS curve fitting (**Figure 3f**, **Figure S3-4** and **Table S1**) demonstrate that the coordination numbers (CN) of the O, S and Ni atoms for Ni are calculated to be 3.8, 2.4 and 4.8, respectively. Based on the above characterizations, it is reasonable to conclude that Ni species in Ni/CdS/Ti$_3$C$_2$T$_x$ are dispersed in two forms, one as single Ni atoms anchored with O atoms in Ti$_3$C$_2$T$_x$ support, and the other as Ni clusters embedded into CdS QDs.

Visible-light-driven lactonization of diols to lactones integrated with H$_2$ production

Taking 1,2-benzenedimethanol (1,2-BM) as the substrate, the photocatalytic dehydrogenative lactonization of diols to lactones with concomitant H$_2$ production was carried out under visible light irradiation (**Figure 4a**). **Figure 4b** and **c** show the photocatalytic activities of blank CdS, CdS/Ti$_3$C$_2$T$_x$ and Ni/CdS/Ti$_3$C$_2$T$_x$ composites with different Ni mass ratios (see **Figure S5-7** for the mass spectra of reactant and products). The blank CdS QDs exhibit an extremely low phthalide production rate of 3.4 μmol g^{-1} h^{-1}. Notably, the optimized Ni$_2$/CdS/Ti$_3$C$_2$T$_x$ exhibits remarkably enhanced phthalide generation rate (273.4 μmol g^{-1} h^{-1}), which is 44.8 times that of the CdS/Ti$_3$C$_2$T$_x$ (6.1 μmol g^{-1} h^{-1}), and 80.4 times that of the blank CdS. In addition, the Ni$_2$/CdS/Ti$_3$C$_2$T$_x$ composites have the highest selectivity of 91.6% for phthalide, while the selectivity of blank CdS QDs is only 48.4% under the same conditions. Unlike the negligible phthalide production, the H$_2$ evolution rates of blank CdS and CdS/Ti$_3$C$_2$T$_x$ reach 105.0 and 338.3 μmol g^{-1} h^{-1}, respectively. These results deduce that although the

8

dehydrogenation of 1,2-BM occurs smoothly to afford protons for H_2 production, the insufficient cyclization capacity of blank CdS and CdS/$Ti_3C_2T_x$ restricts the phthalide generation, as will be discussed later. In contrast, the molar ratio of oxidation product (phthalide and o-phthaladehyde) and reduction product (H_2) over Ni_2/CdS/$Ti_3C_2T_x$ is calculated to be approximately 1:2.9. The slight deviation from the stoichiometric ratio (1:2) of such lactonization reaction may be attributed to the difference in thermodynamics and kinetics of the two half-reactions.[2] Time profiles in **Figure S8** show that the production of phthalide over Ni_2/CdS/$Ti_3C_2T_x$ composite increases along with the light irradiation time. In addition, this system is also quite compatible with other aromatic diols (**Table S2**). Moreover, the calculated apparent quantum yield (AQY) of Ni_2/CdS/$Ti_3C_2T_x$ composite is closely related to the wavelength of incident light and well matches its diffuse reflectance spectroscopy (DRS) spectrum (**Figure 4d**).

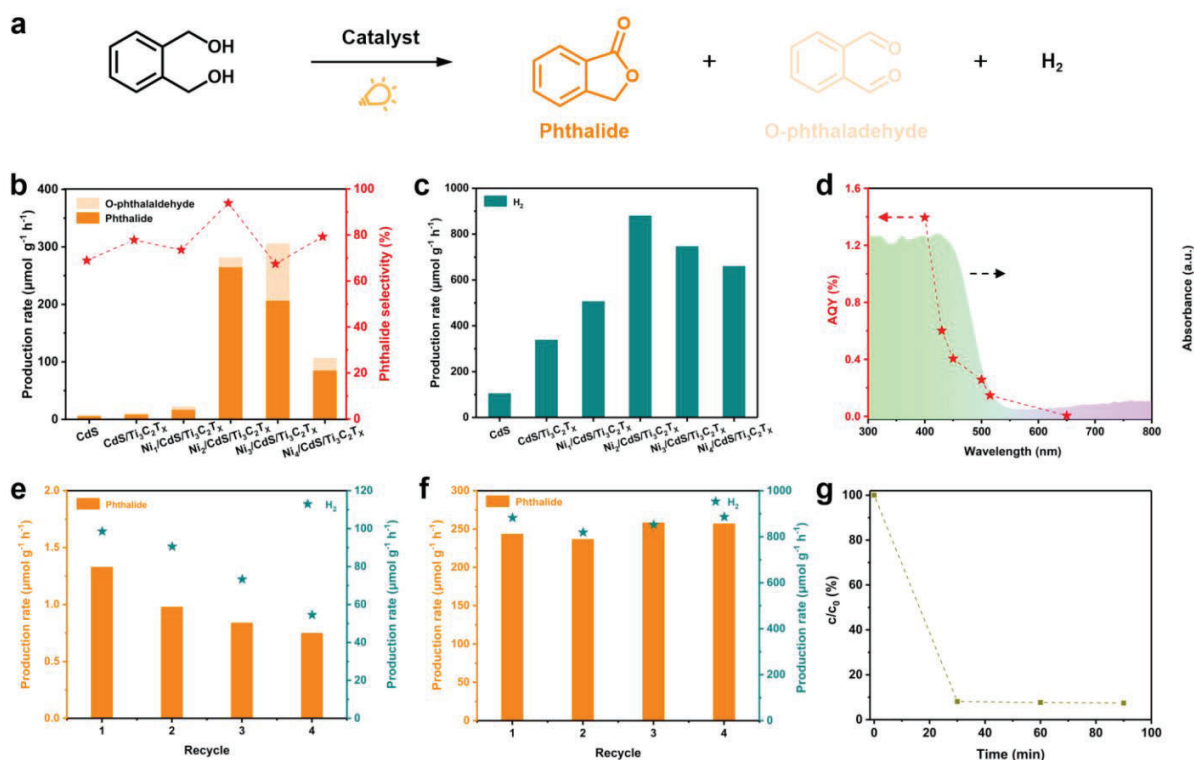**Figure 4.** (a) The illustration for the visible-light-driven lactonization of 1,2-BM to phthalide integrated with H_2 production. (b) Production rate of various products and phthalide selectivity over CdS, CdS/$Ti_3C_2T_x$ and Ni/CdS/$Ti_3C_2T_x$. (c) H_2 production rate over CdS, CdS/$Ti_3C_2T_x$ and Ni/CdS/$Ti_3C_2T_x$. (d) DRS spectrum of Ni_2/CdS/$Ti_3C_2T_x$ and AQYs for phthalide production over

$Ni_2/CdS/Ti_3C_2T_x$ under different monochromatic lights. Recycling tests over (e) CdS QDs and (f) $Ni_2/CdS/Ti_3C_2T_x$. (g) Adsorption of Cd^{2+} over $Ti_3C_2T_x$ NSs in the dark.

Reusability experiment was carried out to verify the stability of photocatalysts. As depicted in **Figure 4e**, the blank CdS QDs show an obvious decrease of 43.6% for phthalide production after four repeated trials. In contrast, no obvious deactivation phenomenon of phthalide and H_2 production can be observed over the $Ni_2/CdS/Ti_3C_2T_x$ (**Figure 4f**). To understand the effect of $Ti_3C_2T_x$ on the enhanced photostability of CdS QDs, Cd^{2+} leaching experiment under visible light irradiation was first measured, as shown in **Table S3**. The leakage of Cd^{2+} in CdS QDs is 20.9 μg g^{-1} after 12 h of light irradiation, while the Cd^{2+} leakage from $Ni_2/CdS/Ti_3C_2T_x$ composites is only 2.6 μg g^{-1}, indicating that the photocorrosion of CdS QDs can be significantly suppressed upon immobilizing on $Ti_3C_2T_x$ NSs. In addition, the Cd^{2+} adsorption experiment was carried out in the dark (**Figure 4g**), and a Cd^{2+} uptake of 46.3 mg g^{-1} is obtained over $Ti_3C_2T_x$ NSs. These data confirm that the loading of CdS QDs onto the $Ti_3C_2T_x$ NSs facilitates the recovery of CdS QDs for reuse, while the Cd^{2+} confinement effect of $Ti_3C_2T_x$ NSs further inhibits the hole-induced photocorrosion of CdS QDs,[29] thus endowing $Ni_2/CdS/Ti_3C_2T_x$ composites with high stability and recyclability.

Mechanism insight for dehydrogenative lactonization of 1,2-BM

Generally, the charge separation/transfer efficiency significantly impacts the catalytic performance of the photoredox system, and therefore, a series of electrochemical/photoelectrochemical characterizations and photoluminescence (PL) spectroscopy were conducted. As shown in **Figure 5a**, the transient photocurrent response of the samples increases in the following order: $Ni/CdS/Ti_3C_2T_x$ > $CdS/Ti_3C_2T_x$ > CdS, suggesting the higher charge separation efficiency in $Ni/CdS/Ti_3C_2T_x$ composites, which was further corroborated by the electrochemical impedance spectroscopy (EIS) spectra (**Figure S9**). The hydrogen evolution reaction (HER) performances of different samples were then investigated by the linear sweep voltammetry (LSV) curves. In **Figure 5b**, the current density remains nearly the same between CdS and $CdS/Ti_3C_2T_x$. Upon decorating with Ni, a noteworthy increase in current density can be observed in the $Ni/CdS/Ti_3C_2T_x$, indicating that the introduction of Ni species promotes the reduction of protons to H_2.[39] The fate of photogenerated charge carriers was further investigated by steady-state photoluminescence (PL) measurements. As sketched in **Figure 5c**,

the PL spectra of different samples display similar emission peak located near 670 nm under monochromatic excitation of 468 nm,[38] and an obvious PL quenching phenomenon appears in CdS/Ti$_3$C$_2$T$_x$, which is mainly attributed to the more efficient inhibition of the charge carrier recombination occurred over CdS/Ti$_3$C$_2$T$_x$ and increased inner scattering upon loaded onto the Ti$_3$C$_2$T$_x$ support. Moreover, a slight blue shift can be observed in the PL spectrum of CdS/Ti$_3$C$_2$T$_x$ composites, suggesting the interaction between CdS QDs and Ti$_3$C$_2$T$_x$ support. Upon decorating with Ni species, a further PL quenching phenomenon can be found in Ni/CdS/Ti$_3$C$_2$T$_x$, confirming the more efficient inhibition of the charge carrier recombination occurred over Ni/CdS/Ti$_3$C$_2$T$_x$. These results verify that the modification of CdS QDs with Ti$_3$C$_2$T$_x$ NSs and Ni species effectively inhibits the recombination of photogenerated carrier charges, and the Ni clusters embedded into CdS QDs could serve as active sites for H$_2$ production, thereby improving the photocatalytic performance of Ni/CdS/Ti$_3$C$_2$T$_x$ composites.

To gain insight into the interface interaction between substrate molecule (1,2-BM) and catalysts, Fourier transform infrared (FTIR) spectroscopy was used to evaluate the adsorption capacity of 1,2-BM on the surface of the samples. As shown in **Figure 5d**, no peaks attributed to 1,2-BM can be observed over CdS, indicating a poor adsorption capacity of 1,2-BM. In a distinct contrast, a strong characteristic peak in the range of 2950–3750 cm^{-1} emerges over Ti$_3$C$_2$T$_x$, which is in agreement with the stretching vibrations of O–H bond in 1,2-BM (**Figure S10**). Besides, the other two peaks located in the range of 700–950 and 2600–2950 cm^{-1}, are corresponding to R–CH$_2$–R and ortho-substitution of the benzene ring in 1,2-BM,[40-41] respectively, further evidencing the strong adsorption capacity of 1,2-BM on the surface of Ti$_3$C$_2$T$_x$. After the introduction of CdS QDs and Ni species on Ti$_3$C$_2$T$_x$, the Ni/CdS/Ti$_3$C$_2$T$_x$ composites still retain excellent adsorption capacity of 1,2-BM. Furthermore, we employed pyridine adsorption FTIR spectroscopy to examine the surface acid strength of catalyst (**Figure S11**). The adsorption peaks at around 1449 and 1540 cm^{-1} arise from pyridine adsorbed on strong Lewis and Brönsted acid sites, respectively.[42] Another peak at 1489 cm^{-1} is attributed to both strong Lewis acid and Brönsted acid sites.[32] As listed in **Table S4**, the ratio of Brönsted and Lewis acid sites (B/L) is near zero, suggesting a dominant role of Lewis acid sites in these catalysts. Significantly, Ti$_3$C$_2$T$_x$ exhibits a greater presence of Lewis acid sites in comparison to CdS. These results suggest that the strong Lewis acid sites present in Ti$_3$C$_2$T$_x$ play a crucial role in the efficient adsorption of 1,2-BM.
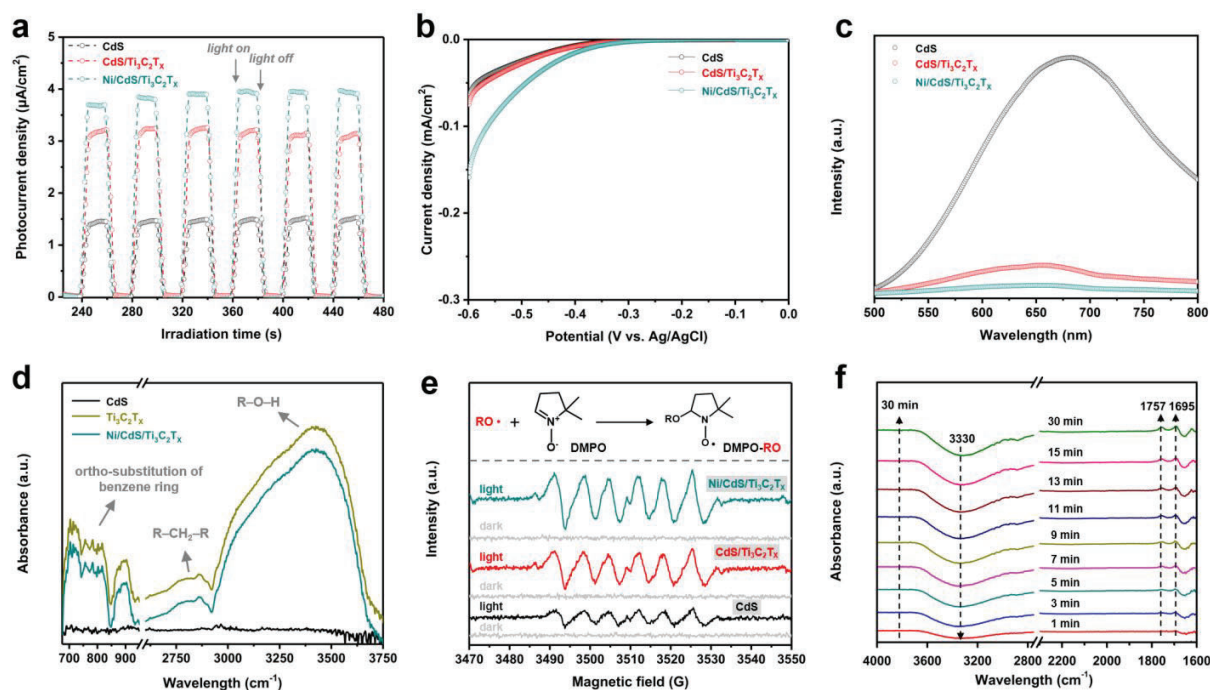
Figure 5. (a) Transient photocurrent responses, (b) LSV curves and (c) PL spectra of CdS, CdS/Ti$_3$C$_2$T$_x$ and Ni/CdS/Ti$_3$C$_2$T$_x$. (d) FTIR spectra of adsorbed 1,2-BM on different photocatalyst samples after the desorption process. (e) In-situ EPR spectra of CdS, CdS/Ti$_3$C$_2$T$_x$ and Ni/CdS/Ti$_3$C$_2$T$_x$ in Ar saturated CH$_3$CN solution in the presence of DMPO and 1,2-BM. (f) In-situ FTIR spectra for the photocatalytic lactonization of 1,2-BM over Ni/CdS/Ti$_3$C$_2$T$_x$.

To explore the reaction mechanism for the dehydrogenative lactonization of 1,2-BM to phthalide integrated with H$_2$ production in the present catalytic system, the band structure of CdS QDs was measured. The bandgap (E$_g$) of CdS QDs is estimated to be 2.32 eV based on the Tauc plot (**Figure S12a**). According to Mott-Schottky analysis (**Figure S12b**), the conduction band minimum (CBM) of CdS QDs is calculated to be –0.65 V *vs.* normal hydrogen electrode (NHE), and the valence band maximum (VBM) of CdS QDs is therefore evaluated to be 1.67 V *vs.* NHE. In addition, the redox potential of 1,2-BM is evaluated to be approximately 1.16 V *vs.* NHE according to the cyclic voltammogram results (**Figure S12c**). Obviously, the CBM of CdS QDs is more negative than E(H$^+$/H$_2$) (–0.41 V *vs.* NHE), and VBM is more positive than E(C$_8$H$_{10}$O$_2$/C$_8$H$_{10}$O$_2$$^{•+}$), which satisfies the thermodynamic constraints for these two half-reactions to proceed simultaneously (**Figure S12d**).[2] To gain further insights, a set of control experiments was carried out under different reaction conditions (**Figure S13**). The reaction

12

cannot proceed in the absence of visible light or photocatalyst, suggesting a photocatalyst-driven reaction process powered by visible light. The addition of CCl_4 as an electron scavenger restrains the H_2 production, while adding triethanolamine (TEOA) as a hole scavenger significantly inhibits the formation of phthalide, indicating the cooperative participation of photoexcited electrons and holes for H_2 and phthalide production. In addition, the addition of 5,5-dimethyl-1-pyrroline-N-oxide (DMPO) as a radical scavenger completely ceases the generation of phthalide, indicating that the phthalide is generated through a radical intermediate.

To identify the radical intermediates generated in the dehydrogenative lactonization of 1,2-BM, in-situ electron paramagnetic resonance (EPR) spectroscopy was performed using DMPO as a trapping agent. As shown in **Figure 5e**, the EPR spectra of all samples under illumination conditions exhibit six characteristic signal peaks (see **Figure S14** for quantitative analysis) belonging to the spin adducts of DMPO and oxygen-centered radicals (i.e., $\cdot O_2H_9C_8$ and $\cdot O_2H_7C_8$ radicals).[43-44] In addition, the DMPO-$O_2H_9C_8$ and DMPO-$O_2H_7C_8$ spin adducts are further confirmed by liquid chromatography-mass (LC-MS) spectrometry (**Figure S15**). It is worth mentioning that both CdS and CdS/$Ti_3C_2T_x$ also exhibit recognizable signal peaks, albeit with slightly lower intensities, indicating that dehydrogenation of 1,2-BM can proceed smoothly in these two catalysts due to the sufficient oxidation capability of the holes photogenerated over the CdS QDs.

In-situ FTIR spectroscopy was employed to further unveil the synthetic pathway of phthalide. As sketched in **Figure 5f**, the absorption peak at 3330 cm^{-1} is attributed to the stretching vibration of O–H bond in the adsorbed 1,2-BM, and the intensity of this peak increases with time, demonstrating the continuous consumption of 1,2-BM under visible light irradiation. The peak at 1695 cm^{-1} is assigned to the stretching vibration of C=O bond (aldehydes),[45] uncovering the gradual formation of aldehydes intermediates (such as $\cdot O_2H_7C_8$ radicals and 2-(hydroxymethyl)-benzaldehyde). Besides, another ever-increasing FTIR peak at 1757 cm^{-1} arise from the stretching vibration of the C=O bond (esters) [46], demonstrating the formation of phthalide during the photocatalytic lactonization process.
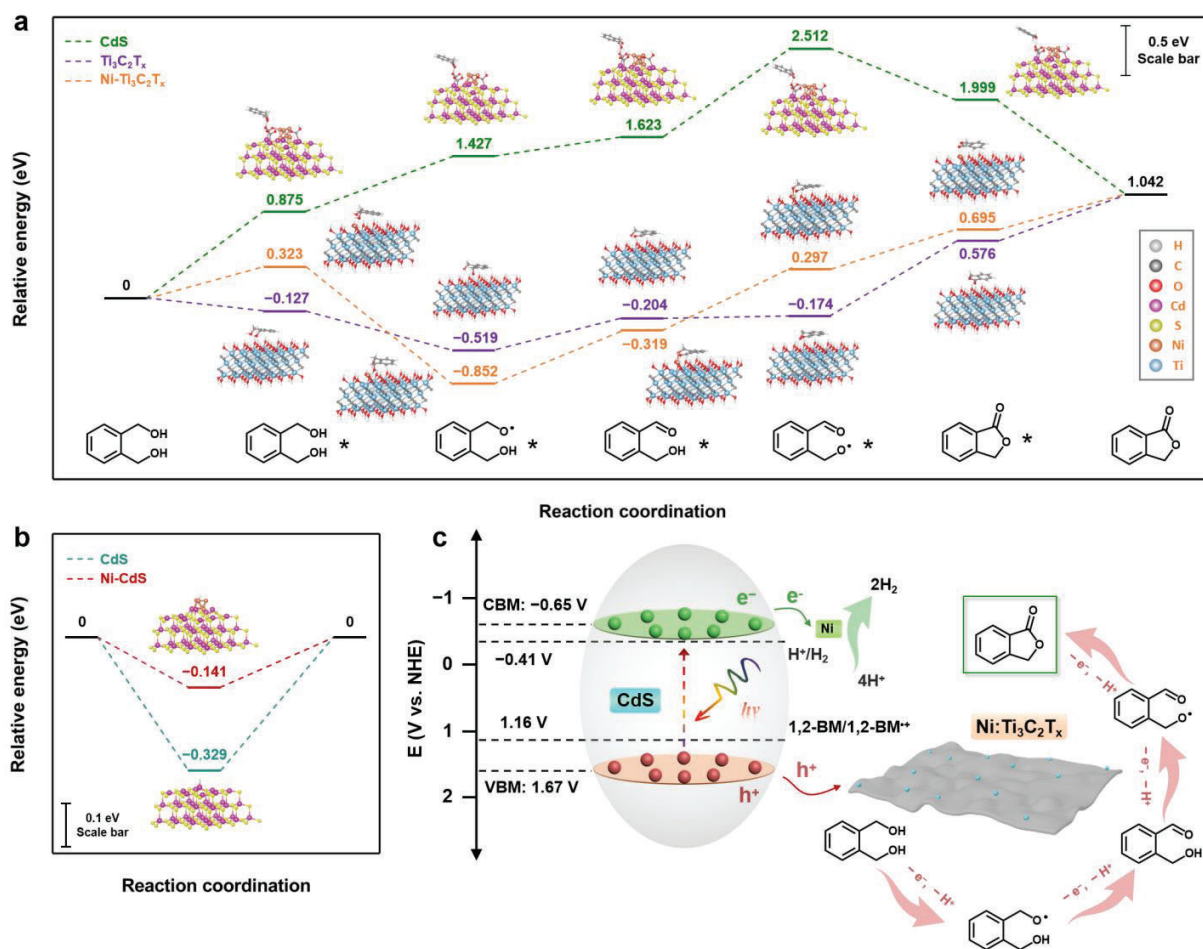
Figure 6. Calculated potential energy diagrams for (a) dehydrogenative lactonization of 1,2-BM and (b) H_2 evolution. (c) Proposed reaction mechanism for photocatalytic phthalide synthesis and H_2 evolution over $Ni/CdS/Ti_3C_2T_x$.

To further gain insights into the overall reaction pathways for the dehydrogenative lactonization of 1,2-BM to phthalide, density functional theory (DFT) calculations were performed (**Figure S16-20**). As depicted in **Figure 6a**, 1,2-BM adsorption step over CdS is endergonic by a high energy barrier of 0.875 eV; nevertheless, such adsorption process is spontaneous on the surface of $Ti_3C_2T_x$ (−0.127 eV), which is agreement with the conclusion drawn from the experimental results. Subsequently, the surface-adsorbed 1,2-BM on $Ti_3C_2T_x$ undergoes successive deprotonation steps with the moderate C/O–H bond cleavage energies of −0.392, 0.315 and 0.030 eV, respectively. It is noteworthy that the ensuring cyclization process of $\bullet O_2H_7C_8$ radicals is significantly harder thermodynamically with a high energy barrier of

14

0.750 eV. Upon decorating with Ni, the cyclization of $\cdot O_2H_7C_8$ radicals intermediate can occur smoothly to produce phthalide by overcoming a moderate energy barrier of 0.398 eV. In addition, the Gibbs free energy (ΔGH^*) for hydrogen adsorption over pristine CdS and Ni-CdS was also investigated. It is widely accepted that the optimal ΔGH^* value should be close to 0 eV for H_2 evolution.[47] As disclosed in **Figure 6b**, the ΔGH^* of pristine CdS QDs is deduced to be -0.329 eV, validating strong hydrogen adsorption on CdS QDs. In contrast, H^+ can adsorb at the Ni clusters embedded into CdS QDs with a low adsorption energy of about -0.141 eV, thus enabling faster formation and release of H_2.

Upon gathering the above information, the overall reaction mechanism of dehydrogenative lactonization of 1,2-BM to phthalide integrated with concomitant H_2 production has been proposed accordingly in **Figure 6c**. Upon visible light irradiation, photogenerated charge carriers are generated from the photoexcition of CdS QDs in $Ni/CdS/Ti_3C_2T_x$. The interfacial interaction between CdS QDs and $Ti_3C_2T_x$ NSs or Ni clusters significantly expedites photoinduced charge carrier separation. Subsequently, the photogenerated holes tend to migrate from CdS to $Ti_3C_2T_x$,[48-49] and then facilely oxidize surface-adsorbed 1,2-BM to produce $\cdot O_2H_9C_8$ radical, which undergoes successive deprotonation steps to afford $\cdot O_2H_7C_8$ radical. Finally, the formed $\cdot O_2H_7C_8$ radical moiety attacks the carbonyl carbon to generate phthalide, which is assisted by the Ni single-atoms sites. Meanwhile, the protons abstracted from 1,2-BM readily interact with photogenerated electrons for H_2 evolution catalysed by the Ni clusters embedded into CdS QDs.

Conclusions

In summary, we showcase the efficient visible-light-driven dehydrogenative lactonization of 1,2-BM to phthalide concomitantly with H_2 production over $Ni/CdS/Ti_3C_2T_x$. Specifically, the $Ti_3C_2T_x$ NSs not only facilitate the separation and transfer of charge carriers from the photoexcitation of CdS QDs, but also supply Lewis acid sites for the efficient adsorption of 1,2-BM. Further Ni modifications are either incorporated as Ni clusters in CdS QDs to accelerate H_2 evolution, or anchored as Ni single atom on $Ti_3C_2T_x$ NSs for the efficient cyclization of 1,2-BM. As a result, the $Ni/CdS/Ti_3C_2T_x$ composites exhibit distinctly boosted photoactivity for phthalide production, which is 80.4 times higher than that of unmodified CdS QDs. In particular, the Cd^{2+} confinement effect of $Ti_3C_2T_x$ significantly slows down the hole-induced photocorrosion of CdS, thus endowing $Ni/CdS/Ti_3C_2T_x$ composites with excellent durability. This work highlights an

avenue for lactones synthesis and offers instructive guidance on the rational design of multifunctional semiconductor-based photocatalysts for highly efficient and recyclable organic synthesis integrated with H_2 generation.

Methods

Synthesis of $Ti_3C_2T_x$ NSs. Typically, HCl (20 mL, 9 mol/L) was first added to a Teflon tube before LiF (1.6 g) was added in batches to a Teflon tube and stirred until the solution became clear, followed by a batch addition of Ti_3AlC_2 powder (1 g) while stirring under an ice bath. After stirring for 10 min, the Teflon tube was transferred to an oil bath for etching for 24 h at 35 °C. The resulting multilayered $Ti_3C_2T_x$ was washed with DI water to pH > 6 and then dissolved in ethanol for sonication for 1 h to delaminate $Ti_3C_2T_x$. After the delaminated $Ti_3C_2T_x$ solution was centrifuged at 10000 rpm for 10 min, the precipitate was collected with DI water by sonication for 1 h. The $Ti_3C_2T_x$ solution was subsequently centrifuged at 3500 rpm for 5 min, and the precipitate was collected and dried in vacuum to obtain single layer of $Ti_3C_2T_x$.

Synthesis of $Ni/CdS/Ti_3C_2T_x$. Typically, 1 mmol of $CdCl_2 \cdot 2.5H_2O$ and 1.7 mmol of MPA were mixed in 20 mL of DI water and the pH was adjusted to about 10 by dropwise adding NaOH solution. A certain amount of $Ti_3C_2T_x$ was added into the solution and stirred for 15 min, then a certain mass ratio (0.125%, 0.25%, 0.5% or 1%) of $NiCl_2$ was dispersed in the solution, and then stirred for 15 min. The solution was transferred into a 50 mL three-necked flask, in which the air was pumped off and replaced with Ar. Under magnetic stirring, 5 mL of Na_2S solution (0.2 M) was injected into the mixture solution. Subsequently, the reaction mixture was heated to 100 °C in an oil bath equipped with a condenser. Finally, when the temperature reached 100 °C, the bright yellow transparent solution was stirred for about 0.5 h. After the solution was cooled, the product was washed with ethanol precipitation and then dried in an oven at 60 °C. The prepared four samples were labeled as $Ni_1/CdS/Ti_3C_2T_x$, $Ni_2/CdS/Ti_3C_2T_x$, $Ni_3/CdS/Ti_3C_2T_x$ and $Ni_4/CdS/Ti_3C_2T_x$, respectively.

Photoactivity testing. In a typical process, 10 mg of sample was added to 10 mL of CH_3CN solution containing 50 μmol of 1,2-BM in a double-wall quartz reaction tube equipped with a condenser water device. Before irradiation, the suspension was sonicated and then purified with Ar for 15 min to completely remove the air. A Xe lamp (PLS-SXE 300D, Beijing Perfectlight

Co., Ltd.) was used as the illumination source. In addition to the reaction conditions that need to be changed, the operating conditions of the control experiment are similar to those of the above photocatalytic methods. The recycling test was operated as follows: after the end of the first round of photocatalytic reaction, the used photocatalyst was separated and washed with absolute ethanol, and then dried in a vacuum oven. The isolated photocatalyst was dispersed into 10 mL of fresh CH_3CN reaction solution containing 0.1 mmol of 1,2-BM for the second activity test. Subsequent recycling tests were also performed similarly. After the reaction, the gas product was analyzed by a gas chromatograph (Shimadzu GC-8A 2014C). The liquid products were monitored by gas chromatography-mass spectroscopy (Shimadzu GC-MS QP 2020, Q-Exactive).

ASSOCIATED CONTENT

Supporting Information. Additional experimental details, characterization and photoactivity results. This material is available free of charge via the Internet at http://pubs.acs.org.

AUTHOR INFORMATION

Corresponding Author

Yi-Jun Xu — College of Chemistry, State Key Laboratory of Photocatalysis on Energy and Environment, Fuzhou University, Fuzhou, 350116, P. R. China; orcid.org/0000-0002-2195-1695; Email: yjxu@fzu.edu.cn; Homepage: http://xugroup.fzu.edu.cn.

Authors

Ming-Yu Qi — Institute of Fundamental and Frontier Sciences, University of Electronic Science and Technology of China, Chengdu 611731, P. R. China; orcid.org/0000-0003-3937-1987

Wei-Yun Xiao — College of Chemistry, State Key Laboratory of Photocatalysis on Energy and Environment, Fuzhou University, Fuzhou, 350116, P. R. China

Marco Conte — Department of Chemistry, University of Sheffield, Sheffield, S3 7HF, UK; orcid.org/0000-0002-1399-0344

Zi-Rong Tang — College of Chemistry, State Key Laboratory of Photocatalysis on Energy and Environment, Fuzhou University, Fuzhou, 350116, P. R. China; orcid.org/0000-0002-6564-3539

Author Contributions

Y.-J.X. proposed the research direction and supervised the project. M.-Y.Q. and W.-Y.X. designed and performed the experiments. M.-Y.Q. and Y.-J.X. wrote and revised the manuscript. Z.-R.T. and M.C. provided helpful suggestions. All authors participated in discussion and reviewed the paper before submission.

Notes

The authors declare no competing financial interest.

REFERENCES

1. Crabtree, R. H., Homogeneous Transition Metal Catalysis of Acceptorless Dehydrogenative Alcohol Oxidation: Applications in Hydrogen Storage and to Heterocycle Synthesis. *Chem. Rev.* **2017,** *117*, 9228-9246.

2. Qi, M.-Y.; Conte, M.; Anpo, M.; Tang, Z.-R.; Xu, Y.-J., Cooperative coupling of oxidative organic synthesis and hydrogen production over semiconductor-based photocatalysts. *Chem. Rev.* **2021,** *121*, 13051-13085.

3. Li, Q.; Jiao, Y.; Tang, Y.; Zhou, J.; Wu, B.; Jiang, B.; Fu, H., Shear Stress Triggers Ultrathin-Nanosheet Carbon Nitride Assembly for Photocatalytic H_2O_2 Production Coupled with Selective Alcohol Oxidation. *J. Am. Chem. Soc.* **2023,** *145*, 20837-20848.

4. Chai, Z.; Zeng, T.-T.; Li, Q.; Lu, L.-Q.; Xiao, W.-J.; Xu, D., Efficient Visible Light-Driven Splitting of Alcohols into Hydrogen and Corresponding Carbonyl Compounds over a Ni-Modified CdS Photocatalyst. *J. Am. Chem. Soc.* **2016,** *138*, 10128-10131.

5.   Sun, X.; Luo, X.; Zhang, X.; Xie, J.; Jin, S.; Wang, H.; Zheng, X.; Wu, X.; Xie, Y., Enhanced Superoxide Generation on Defective Surfaces for Selective Photooxidation. *J. Am. Chem. Soc.* **2019,** *141*, 3797-3801.

6.   Lang, X.; Ma, W.; Chen, C.; Ji, H.; Zhao, J., Selective Aerobic Oxidation Mediated by TiO_2 Photocatalysis. *Acc. Chem. Res.* **2014,** *47*, 355-363.

7.   Kasap, H.; Caputo, C. A.; Martindale, B. C. M.; Godin, R.; Lau, V. W.-h.; Lotsch, B. V.; Durrant, J. R.; Reisner, E., Solar-Driven Reduction of Aqueous Protons Coupled to Selective Alcohol Oxidation with a Carbon Nitride–Molecular Ni Catalyst System. *J. Am. Chem. Soc.* **2016,** *138*, 9183-9192.

8.   Lin, Q.; Li, Y.-H.; Qi, M.-Y.; Li, J.-Y.; Tang, Z.-R.; Anpo, M.; Yamada, Y. M. A.; Xu, Y.-J., Photoredox dual reaction for selective alcohol oxidation and hydrogen evolution over nickel surface-modified $ZnIn_2S_4$. *Appl. Catal., B* **2020,** *271*, 118946.

9.   Li, H.; Qin, F.; Yang, Z.; Cui, X.; Wang, J.; Zhang, L., New Reaction Pathway Induced by Plasmon for Selective Benzyl Alcohol Oxidation on BiOCl Possessing Oxygen Vacancies. *J. Am. Chem. Soc.* **2017,** *139*, 3513-3521.

10.   Xie, S.; Shen, Z.; Deng, J.; Guo, P.; Zhang, Q.; Zhang, H.; Ma, C.; Jiang, Z.; Cheng, J.; Deng, D.; Wang, Y., Visible light-driven C-H activation and C-C coupling of methanol into ethylene glycol. *Nat. Commun.* **2018,** *9*, 1181.

11.   Qi, M.-Y.; Li, Y.-H.; Anpo, M.; Tang, Z.-R.; Xu, Y.-J., Efficient photoredox-mediated C–C coupling organic synthesis and hydrogen production over engineered semiconductor quantum dots. *ACS Catal.* **2020,** *10*, 14327-14335.

12.   Luo, N.; Hou, T.; Liu, S.; Zeng, B.; Lu, J.; Zhang, J.; Li, H.; Wang, F., Photocatalytic Coproduction of Deoxybenzoin and H_2 through Tandem Redox Reactions. *ACS Catal.* **2020,** *10*, 762-769.

13.   Li, J.-Y.; Li, Y.-H.; Zhang, F.; Tang, Z.-R.; Xu, Y.-J., Visible-light-driven integrated organic synthesis and hydrogen evolution over 1D/2D CdS-$Ti_3C_2T_x$ MXene composites. *Appl. Catal., B* **2020,** *269*, 118783.

14.   Wang, L.; Sun, Y.; Zhang, F.; Hu, J.; Hu, W.; Xie, S.; Wang, Y.; Feng, J.; Li, Y.; Wang, G.; Zhang, B.; Wang, H.; Zhang, Q.; Wang, Y., Precisely Constructed Metal Sulfides with Localized Single-Atom Rhodium for Photocatalytic C−H Activation and Direct Methanol Coupling to Ethylene Glycol. *Adv. Mater.* **2023,** *35*, 2205782.

15.   Han, C.; Zeng, Z.; Zhang, X.; Liang, Y.; Kundu, B. K.; Yuan, L.; Tan, C.-L.; Zhang, Y.; Xu, Y.-J., All-in-One: Plasmonic Janus Heterostructures for Efficient Cooperative Photoredox Catalysis. *Angew. Chem. Int. Ed.* **2024,** *n/a*, e202408527.

16.   Wackelin, D. J.; Mao, R.; Sicinski, K. M.; Zhao, Y.; Das, A.; Chen, K.; Arnold, F. H., Enzymatic Assembly of Diverse Lactone Structures: An Intramolecular C–H Functionalization Strategy. *J. Am. Chem. Soc.* **2024,** *146*, 1580-1587.

17.   Ge, Y.; Ye, F.; Liu, J.; Yang, J.; Spannenberg, A.; Jiao, H.; Jackstell, R.; Beller, M., Ligand-Controlled Palladium-Catalyzed Carbonylation of Alkynols: Highly Selective Synthesis of α-Methylene-β-Lactones. *Angew. Chem. Int. Ed.* **2020,** *59*, 21585-21590.

18.   Gao, D.-W.; Jamieson, C. S.; Wang, G.; Yan, Y.; Zhou, J.; Houk, K. N.; Tang, Y., A Polyketide Cyclase That Forms Medium-Ring Lactones. *J. Am. Chem. Soc.* **2021,** *143*, 80-84.

19.   Eberlein, T. H., Essentials of organic chemistry: For students of pharmacy, medicinal chemistry, and biological chemistry (Paul M. Dewick). *J. Chem. Educ.* **2008,** *85*, 204.

20.   Espinosa-Jalapa, N. A.; Kumar, A.; Leitus, G.; Diskin-Posner, Y.; Milstein, D., Synthesis of Cyclic Imides by Acceptorless Dehydrogenative Coupling of Diols and Amines Catalyzed by a Manganese Pincer Complex. *J. Am. Chem. Soc.* **2017,** *139*, 11722-11725.

21.   Xie, X.; Stahl, S. S., Efficient and Selective Cu/Nitroxyl-Catalyzed Methods for Aerobic Oxidative Lactonization of Diols. *J. Am. Chem. Soc.* **2015,** *137*, 3767-3770.

22.   Kinoshita, H.; Shinokubo, H.; Oshima, K., Synthesis of Medium- and Large-Sized Lactones in an Aqueous–Organic Biphasic System. *Angew. Chem., Int. Ed.* **2005,** *44*, 2397-2400.

23.   Cheung, K. P. S.; Sarkar, S.; Gevorgyan, V., Visible Light-Induced Transition Metal Catalysis. *Chem. Rev.* **2022,** *122*, 1543-1625.

24.   Yu, Y.; Chakraborty, P.; Song, J.; Zhu, L.; Li, C.; Huang, X., Easy access to medium-sized lactones through metal carbene migratory insertion enabled 1,4-palladium shift. *Nat. Commun.* **2020,** *11*, 461.

25.   Li, X.-B.; Tung, C.-H.; Wu, L.-Z., Semiconducting quantum dots for artificial photosynthesis. *Nat. Rev. Chem.* **2018,** *2*, 160-173.

26.   Xia, T.; Gong, W.; Chen, Y.; Duan, M.; Ma, J.; Cui, X.; Dai, Y.; Gao, C.; Xiong, Y., Sunlight-driven highly selective catalytic oxidation of 5-Hydroxymethylfurfural towards tunable products. *Angew. Chem., Int. Ed.* **2022,** *61*, e202204225.

27.   Wu, X.; Fan, X.; Xie, S.; Lin, J.; Cheng, J.; Zhang, Q.; Chen, L.; Wang, Y., Solar energy-driven lignin-first approach to full utilization of lignocellulosic biomass under mild conditions. *Nat. Catal* **2018,** *1*, 772-780.

28.   Qi, M.-Y.; Conte, M.; Tang, Z.-R.; Xu, Y.-J., Engineering semiconductor quantum dots for selectivity switch on high-performance heterogeneous coupling photosynthesis. *ACS Nano* **2022,** *16*, 17444-17453.

29.   Xie, X.; Zhang, N.; Tang, Z.-R.; Anpo, M.; Xu, Y.-J., $Ti_3C_2T_x$ MXene as a Janus cocatalyst for concurrent promoted photoactivity and inhibited photocorrosion. *Appl. Catal., B* **2018,** *237*, 43-49.

30.   Xie, X.; Chen, C.; Zhang, N.; Tang, Z.-R.; Jiang, J.; Xu, Y.-J., Microstructure and surface control of MXene films for water purification. *Nat. Sustain.* **2019,** *2*, 856-862.

31.   Ran, J.; Gao, G.; Li, F.-T.; Ma, T.-Y.; Du, A.; Qiao, S.-Z., Ti_3C_2 MXene co-catalyst on metal sulfide photo-absorbers for enhanced visible-light photocatalytic hydrogen production. *Nat. Commun.* **2017,** *8*, 13907.

32.   Fei, X.; Wang, Y.; Guo, P.; Wang, J.; Wang, G.; Lu, G.; Zhao, W.; Liu, X., Efficient Catalytic Activity of $Ti_3C_2T_x$ MXene for Polyester Synthesis. *Ind. Eng. Chem. Res.* **2024,** *63*, 6868-6879.

33.   Li, M.; Lu, J.; Luo, K.; Li, Y.; Chang, K.; Chen, K.; Zhou, J.; Rosen, J.; Hultman, L.; Eklund, P.; Persson, P. O. Å.; Du, S.; Chai, Z.; Huang, Z.; Huang, Q., Element Replacement Approach by Reaction with Lewis Acidic Molten Salts to Synthesize Nanolaminated MAX Phases and MXenes. *J. Am. Chem. Soc.* **2019,** *141*, 4730-4737.

34.   Liang, J.; Zhang, Q.; Zhao, H.; Zhao, S.; Wu, Y.; Fan, X., Hydrodeoxygenation of Palmitic Acid with Novel Two-Dimensional $Ti_3C_2T_x$ MXene-Supported Ni Catalyst. *Ind. Eng. Chem. Res.* **2022,** *61*, 13275-13282.

35.   Li, S.; Su, M.; Sun, J.; Hu, K.; Jin, J., Visible Light-Promoted Magnesium, Iron, and Nickel Catalysis Enabling C(sp^3)–H Lactonization of 2-Alkylbenzoic Acids. *Org. Lett.* **2021,** *23*, 5842-5847.

36.   Chen, Y.-H.; Qi, M.-Y.; Li, Y.-H.; Tang, Z.-R.; Wang, T.; Gong, J.; Xu, Y.-J., Activating two-dimensional $Ti_3C_2T_x$-MXene with single-atom cobalt for efficient CO_2 photoreduction. *Cell Rep. Phys. Sci.* **2021,** *2*, 100371.

37.   Yang, H. B.; Hung, S.-F.; Liu, S.; Yuan, K.; Miao, S.; Zhang, L.; Huang, X.; Wang, H.-Y.; Cai, W.; Chen, R.; Gao, J.; Yang, X.; Chen, W.; Huang, Y.; Chen, H. M.; Li, C. M.; Zhang, T.; Liu, B., Atomically dispersed Ni(i) as the active site for electrochemical CO_2 reduction. *Nat. Energy* **2018,** *3*, 140-147.

38.   Qi, M.-Y.; Xu, Y.-J., Efficient and Direct Functionalization of Allylic sp^3 C−H Bonds with Concomitant CO_2 Reduction. *Angew. Chem., Int. Ed.* **2023,** *62*, e202311731.

39.   Qi, M.-Y.; Li, Y.-H.; Zhang, F.; Tang, Z.-R.; Xiong, Y.; Xu, Y.-J., Switching light for site-directed spatial loading of cocatalysts onto heterojunction photocatalysts with boosted redox catalysis. *ACS Catal.* **2020,** *10*, 3194-3202.

40.   Kanazawa, S.; Yamada, Y.; Sato, S., Infrared spectroscopy of graphene nanoribbons and aromatic compounds with sp^3 C–H (methyl or methylene groups). *J. Mater. Sci.* **2021,** *56*, 12285-12314.

41.   Schuur, J.; Gasteiger, J., Infrared Spectra Simulation of Substituted Benzene Derivatives on the Basis of a 3D Structure Representation. *Anal. Chem.* **1997,** *69*, 2398-2405.

42.   Wang, L.; Wang, H.; Cheng, R.; Wang, M.; Cai, X.; Ren, P.; Xiao, D.; Wang, N.; Wen, X.-D.; Diao, J.; Wang, X.; Ma, D.; Liu, H., High-Density Coordinatively Unsaturated Zn Catalyst for Efficient Alkane Dehydrogenation. *J. Am. Chem. Soc.* **2023,** *145*, 20936-20942.

43. Barthelemy, A.-L.; Tuccio, B.; Magnier, E.; Dagousset, G., Intermolecular trapping of alkoxyl radicals with alkenes: A new route to ether synthesis. *Synlett* **2019,** *30*, 1489-1495.

44. Chen, L.; Duan, J.; Du, P.; Sun, W.; Lai, B.; Liu, W., Accurate identification of radicals by in-situ electron paramagnetic resonance in ultraviolet-based homogenous advanced oxidation processes. *Water Res.* **2022,** *221*, 118747.

45. Zavadskaya, M.; Chizhevskaya, I., Integral intensities of C=O bands in the IR spectra of some aromatic aldehydes. *J. Appl. Spectrosc.* **1970,** *12*, 134-135.

46. Arun, Y.; Ghosh, R.; Domb, A. J., Poly(ester-anhydrides) derived from esters of hydroxy acid and cyclic anhydrides. *Biomacromolecules* **2022,** *23*, 3417-3428.

47. Zhang, J.; Zhao, Y.; Guo, X.; Chen, C.; Dong, C.-L.; Liu, R.-S.; Han, C.-P.; Li, Y.; Gogotsi, Y.; Wang, G., Single platinum atoms immobilized on an MXene as an efficient catalyst for the hydrogen evolution reaction. *Nat. Catal.* **2018,** *1*, 985-992.

48. Peng, C.; Wei, P.; Li, X.; Liu, Y.; Cao, Y.; Wang, H.; Yu, H.; Peng, F.; Zhang, L.; Zhang, B.; Lv, K., High efficiency photocatalytic hydrogen production over ternary $Cu/TiO_2@Ti_3C_2T_x$ enabled by low-work-function 2D titanium carbide. *Nano Energy* **2018,** *53*, 97-107.

49. Peng, C.; Xu, W.; Wei, P.; Liu, M.; Guo, L.; Wu, P.; Zhang, K.; Cao, Y.; Wang, H.; Yu, H.; Peng, F.; Yan, X., Manipulating photocatalytic pathway and activity of ternary $Cu_2O/(001)TiO_2@Ti_3C_2T_x$ catalysts for H_2 evolution: Effect of surface coverage. *Int. J. Hydrogen Energy* **2019,** *44*, 29975-29985.